ORIGINAL RESEARCH ARTICLE

Exploring the Effects of Processing Parameters on the Flexural Performance of Polylactic Acid Fabricated through a Customized High Extrusion Rate Fused Filament Fabrication System

Zhaogui Wang [ORCID], Jinze Wang, Yeshu Zhang, Yuanqing Li, and Yuxuan Li

Fused filament fabrication (FFF) has recently been extended to large-format additive manufacturing (LFAM) systems, which offer substantial advantages for the highly efficient manufacturing of large parts and tools. The aim of this study was to extend the material feeding rate of an open-ended conventional FFF 3D printer, presenting an alternative to the screw extruder-based LFAM systems that are used to date. We investigated the effects of printing parameters, such as nozzle diameter, bead width, and in-plane printing infill direction, on the mechanical performance of processed polylactic acid (PLA) materials. We quantitatively evaluated the mechanical performance of PLA specimens through three-point bending tests. The experimental results demonstrated that the flexural strength and maximum deflection of the FFF specimens are highly sensitive to the parameters of interest, while the flexural stiffness remains stable regardless of variations in parameters. Compared to specimens produced by regular FFF 3D printers, those created using the modified system exhibit 10% increases in bending strength. The extrusion bead width plays a significant role in varying the bending properties of the printed specimens, with maximum differences exceeding 15%. Mesostructural analyses of the interlayer formations of the deposited beads indicated that the layer bead width has a more pronounced effect on the formation of interbead voids than the raster angle, resulting in a more noticeable reduction in mechanical properties.

1. Introduction

Fused filament fabrication (FFF) is considered one of the most popular additive manufacturing (3D printing) methods, owing to its high capacity to fabricate intricate 3D components with less material waste and energy consumption than traditional subtractive manufacturing methods. A typical process of FFF starts with feeding a continuous polymer filament into an extrusion head via a pinch roller feeding mechanism. The solid filament is then melted by the heating block mounted outside the feeding pipe, and the molten polymer is finally extruded through a heated nozzle and deposited onto a preheated material substrate in a layer-by-layer manner to form a specific part. In such cases, it is important to note that the processing parameters of FFFs can significantly influence the mechanical properties of the resulting products (cf. Fig. 1). The build orientation is the primary factor that determines the resulting properties of a printed part. Owing to the inherently weak bonding between the vertically deposited beads, the in-plane material load direction exhibits higher mechanical properties than the out-of-plane material deposition direction. The key parameters that influence the mechanical properties are the raster-to-raster air gap, raster angle, layer thickness, infill density, and build orientation. Given the complex influences of these parameters on the mechanical properties of end parts, it is important to focus on evaluating their joint effect, which corresponds to real manufacturing conditions and applications (Ref 1). Chacón et al. found that the tensile and flexural strengths of printed ABS were significantly reduced along the deposition direction, and the layer thickness and the printing speed directly impacted the mechanical properties of ABS parts (Ref 2). Raut et al. studied the effects of build orientation on the mechanical properties and overall costs of FFF parts. The results showed that the FFF part 0° from the y-axis had good tensile strength and the lowest cost among the investigated specimens. FFF part 0° from the x-axis had good flexural strength and a moderate cost (Ref 3). Rayegani et al. adopted a method involving full factorial design and suggested that the build orientation, air gap, raster angle, and width influenced the tensile strength of the FFF-produced prototype. The optimal technological parameters of the maximum tensile strength were obtained (Ref 4). Sood et al. found that the layer thickness and the raster angle had much greater effects on the residual stress

Zhaogui Wang and Jinze Wang, Department of Mechanical Engineering, Naval Architecture and Ocean Engineering College, Dalian Maritime University, Dalian 116026 Liaoning, China; and Yeshu Zhang, Yuanqing Li, and Yuxuan Li, Houston International Institute, Dalian Maritime University, Dalian 116026 Liaoning, China. Contact e-mail: zhaogui_wang@dlmu.edu.cn.

and deformation than other controllable factors according to a combination analysis of CCD and ANOVA (Ref 5). Mohamed developed mathematical models to predict the processing time, material cost, and mechanical performance and found that the most effective variables were layer thickness, air gap, and build direction (Ref 6). Sood et al. studied the effects of important process parameters, i.e., layer thickness, orientation, raster angle, raster width, and air gap. The responses considered in that study were the mechanical properties of FFF-produced parts, such as tensile, bending, and impact strength (Ref 7).

The finishing quality of 3D-printed parts significantly depends on the process parameters. Narang et al. showed that a smaller layer thickness corresponded to a higher dimensional accuracy and a higher surface quality of a part. Variations in the build orientation and grating angle did not affect the surface finish of FFF-produced parts (Ref 8). Bead width could influence the surface quality and dimensional accuracy (Ref 9). Bahar et al. studied the fluctuation of bead width caused by the inconsistency of the actual feed rate and the extrusion rate (Ref 10). The experimental results of Sun et al. showed that effectively controlling cooling conditions greatly impacted the mechanical properties and accuracy of the final parts manufactured by the FFF process (Ref 11). Khunt et al. found through finite element analysis that a relatively high printing temperature, low printing speed, and narrow layer thickness improved the density and surface finish qualities of printed parts (Ref 12). Wang et al. studied the impacts of several significant process variables on the dimensional accuracy, surface roughness, and tensile strength parameters of acrylonitrile–butadiene–styrene (ABS) copolymer parts and obtained the optimal parameter combination (Ref 13). Torres et al. reported that a slower speed and lower layer thickness led to a higher resolution and better surface quality of PLA (Ref 14). Furthermore, the results of Lei et al. showed that increasing the nozzle temperature and decreasing the nozzle speed increased the thickness and width of the deposited filaments, resulting in an increase in the tensile properties of PLA/GNP samples of 18.6% (Ref 15). Dezaki et al. concluded that honeycomb and checkered patterns were the strongest and most lightweight patterns. The 0° sample had a higher strength and better quality than the vertical sample. Furthermore, the printer could not print at an angle of 75° in the planar direction (Ref 16). Shanmugam et al. concluded that fibers in printed parts increased strength depending on FFF process parameters and filament parameters. Continuous fiber composites had higher strengths than short fiber-reinforced FFF composites (Ref 17). Panda et al. found that layer thickness and extrusion rate affected warpage. The filling speed and bead width compensation had the greatest impact on dimensional errors among the evaluated factors (Ref 18).

In particular, the nozzle diameter is a crucial factor affecting the performance of highly sensitive printed parts. Sukindara et al. found that the nozzle diameter was one of the factors that affected the pressure drop along the liquefier (Ref 19). Kiński et al. found that the fracture force of samples with a packing density of 50% increased with increasing nozzle diameter, while the fracture force of samples with 100% packing density decreased with increasing nozzle diameter (Ref 20). Buj-Corral et al. studied the effects of the nozzle diameter and fill rate on the porosity and pore size values of printed samples (Ref 21). Yang et al. found that the tensile strength and surface roughness increased significantly with increasing nozzle diameter, extru-

sion rate, and filler layer thickness. Increases in the nozzle diameter, filling speed, and layer thickness reduced the build time (Ref 22). Chen et al. used a self-developed print head for printing and concluded that different nozzle vibration frequencies reduced the viscosity of the material and generated downward inertial force, which affected the porosity of the part and enhanced the diffusion of polymer chains, thus increasing the vertical tensile strength (Ref 23). Czyżewski et al. used an extrusion nozzle with a diameter of 0.8 mm to obtain macrostructures with a high number of layers, interconnected paths, and good mechanical properties (Ref 24). Sukindar et al. focused on the effects of the nozzle diameter on the pressure drop, geometric error, and extrusion time. The highest pressure drop was obtained with a 0.2-mm nozzle, but the value was not within the optimal range (Ref 19). Brooks et al. used an additive manufacturing system to provide variable diameter nozzles for polymer fused deposition, optimizing printing resolution (Ref 25). For a given nozzle diameter, the higher the filler content was, the lower the porosity and pore size. In contrast, a larger nozzle diameter indicated a larger distance between the filaments and thus a larger aperture to achieve a certain filling value (Ref 26). For instance, Wu et al. introduced a magnetically controlled nozzle to adjust its outlet diameter under the control of magnetic fields (Ref 27). Monzón et al. introduced a modified nozzle design to the FFF printer, aiming to apply fine resolutions. Their results provided insights into the thermal effects of the materials when reduced diameter nozzles were used (Ref 28). Nakao et al. patented a variable squeeze mouth. The variable cross-section was obtained by moving a nut and/or collet inside the nozzle; thus, the size of the outlet could be adjusted (Ref 29). A study was performed by Ramanath using FEA that observed the flow behavior of polycaprolactone (PCL) by changing the nozzle diameter from 0.2 to 0.4 mm. The results showed that the smaller the diameter was, the higher the pressure drop (Ref 30). Kuznetsov and his team showed that variable nozzle diameters, layer thicknesses, and printing rates, among other factors, could affect the structures obtained. The beneficial effect on the intensity of using a large nozzle diameter (0.8 mm) while keeping the layer thickness thin (0.15 mm) was demonstrated (Ref 31). The samples used for strength tests were printed from the biodegradable PLA (polylactic acid/polylactide) material, which is a polymer obtained from renewable natural raw materials (Ref 32).

Recently, FFF has been extended to large-format additive manufacturing (LFAM) applications, where a screw-based feeding mechanism is used for massive and rapid material deposition. The LFAM system has seen continuous increases in implementations in the automotive, naval, and energy industries for the efficient production of large-dimensional parts with lower costs than traditional approaches. For example, Pignatelli et al. compared large-format additive manufacturing with fused filament fabrication (FFF) and found that LFAM has higher deposition rates and lower material costs than FFF (Ref 33). Nevertheless, with a different system of material feeding, the valuable experiences earned via FFF studies may not be fully applicable, and the processing parameters of LFAM are often calibrated via tedious trial-and-error processes. Moreno et al. revealed the growth of scientific and industrial activities and devices in the field of LFAM. There are still great possibilities for

development and improvement in each area related to LFAM: material development, technology, design, and simulation (Ref 34). Ajinjeru et al. investigated the processing conditions applicable to large-format additive manufacturing systems to ensure that the end part is robust and possesses the desired properties (Ref 35). Specifically, the material extrusion rate is an important parameter in highly efficient 3D printing. Butta et al. investigated the effects of different material extrusion rates on the quality, dimensional accuracy, surface texture, and mechanical properties of. The researchers used different extrusion rates for specific operations according to the product requirements (Ref 36). Geng et al. investigated the effects of the extrusion rate and the printing rate on the microstructures and dimensions of 3D-printed PEEK filaments. The relationship between the extrusion rate and the extruded filament diameter was established by measuring the extruded filament diameter at different extrusion rates (Ref 37). Jin et al. developed a technique for detection and self-correction that detected automatic changes in printing parameters during underextrusion or overextrusion (Ref 38).

In this paper, we simply modify the conventional setup of a desktop size FFF 3D printer, aiming to increase the material loading rate. The nozzle die diameter of the FFF printer is increased from 0.4 mm (conventionally used) to 1 mm, thereby increasing the volume deposition rate and bead dimensions and ultimately increasing the efficiency of the FFF process. To be compatible with the upgraded nozzle, the dimensions of the filament, the pinch roller feed system, and the extrusion heater are modified. We name the resulting system high extrusion rate fused filament fabrication (HFFF) to differentiate it from traditional FFF printers. The HFFF system can provide an increased manufacturing efficiency, thereby yielding advantages in the additive manufacturing of components with substantial dimensions and effectively reducing time consumption. With the HFFF system, we test the effects of the layer bead width on the flexural properties of fabricated polymer and polymer composites. In this case, we note that the bead dimensions of a deposit are affected by the layer thickness, printing speed, and nozzle temperature in a coupled manner. Here, we employ a mono-factor approach that first evaluates the influence of the bead width, which directly determines the in-plane and out-of-plane mesovoid formations between the interbeads. The measured data show that HFFF is a promising method for improving the manufacturing efficiency while maintaining the high product quality of 3D-printed parts.
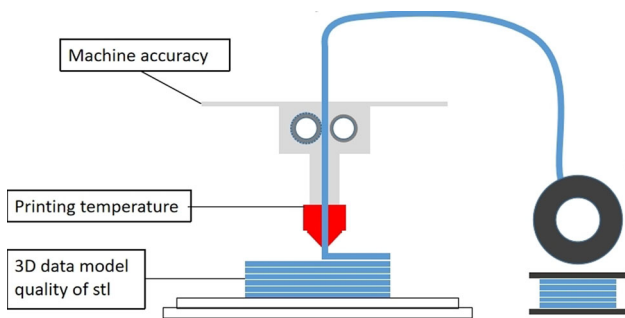

Fig. 1 FFF printing parameters that significantly affect the mechanical performance of products

2. Methods

In this section, we systematically present the HFFF system employed in this study, where the differences between a traditional FFF 3D printer and our revised instrument are provided. In addition, we introduce the feedstock materials applied in the work with the thermal material characterization data that help to determine the processing parameters for bending test specimens.

2.1 HFFF 3D Printing System

The customized HFFF system is revised based on an open-end FFF 3D printer (Shanghai Mingxiang Information Technology Co., Ltd. MX RESEARCH, Shanghai, China). As shown in Fig. 2, a major revision of the HFFF system is a 1-mm nozzle diameter (instead of the traditional 0.4-mm nozzle diameter), which leads to an $\sim 500\%$ increment in the nozzle end cross-section area (i.e., from 0.13 to 0.79 mm^2). To incorporate the flow rate of the nozzle end, the nozzle inlet is enlarged to 3.2 mm, as shown in Fig. 3. Consequently, the diameter of the feedstock filament is 2.85 mm, which is 63% larger than that of the conventional commercial filament (i.e., a diameter of 1.75 mm). The filament rolling gear and associated spring are stiffer than the conventional gear, which provides a large shear force ensuring a stable feeding rate. The extruder of the HFFF is a similar size to the conventional extruder. To melt the filament smoothly and successfully with a large diameter, we upgrade the power of the hot end and increase the extrusion rate. Figure 4 shows a schematic paradigm summarizing the
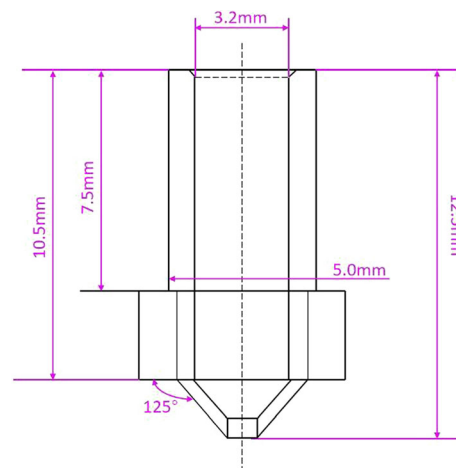

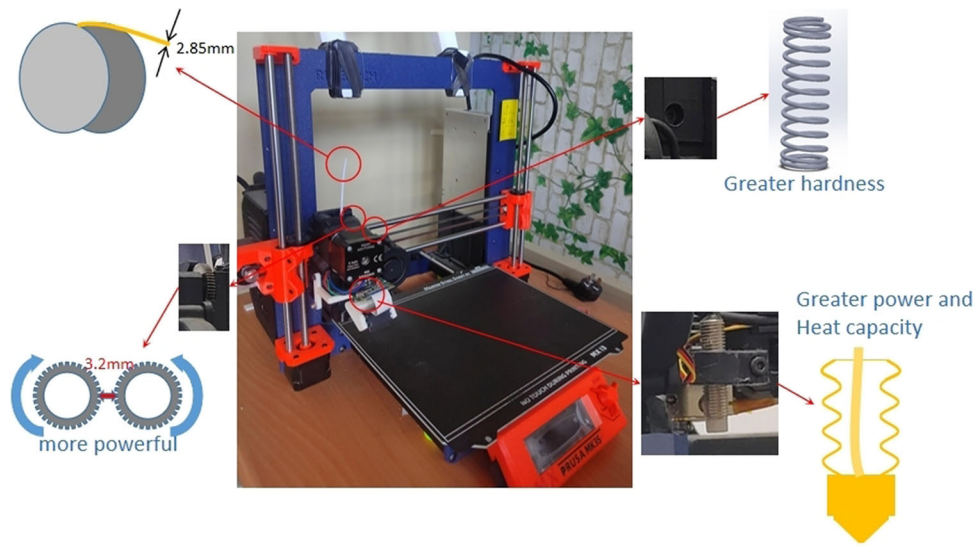**Fig. 2** HFFF 1-mm nozzle diameter

Fig. 3 Nozzle inlet

Fig. 4 Schematic paradigm of the HFFF system setup

Table 1 Differences between conventional FFF and upgraded HFFF systems

Factor	HFFF	FFF
Nozzle diameter	1 mm	0.4 mm
Nozzle end cross-section area	0.79 mm^2	0.13 mm^2
Filament diameter	2.85 mm	1.75 mm
Filament cross-section area	6.38 mm^2	2.41 mm^2
Filament through path size	3.2 mm	2.0 mm
Tooth ratio of the feed gear	3:1	1:1
Spring strength factor	0.98 N/mm	19.5 N/mm
Spring hardness	0.1 kg/mm	2 kg/mm
Extruder hot end heating power	70 W	50 W
Extrusion rate	6.43 g/7 min = 0.92 g/min	6 g/27 min = 0.22 g/min

modifications of the HFFF 3D printing system. In addition, the differences between a conventional FFF printer and our HFFF system are shown in Table 1.

2.2 Material Characterizations

We benchmark the mechanical performance of HFFF-produced PLA specimens via three-point bending tests. The geometry of the bending specimen is designed following the ASTM D790 standard (Ref 39). The printing size and building orientation of the sample are shown in Fig. 5. The three-point bending tests are performed using a CTM 8010 microelectrical all-in-one material tester (Xieqiang Instruments Manufacturer Inc., Shanghai, China), where the fixed stress mode is applied with a loading rate of 100 MPa/s. From preexperiments of the HFFF system, the printing parameters that are directly associated with the deposited beads yield significant impacts on the mechanical properties of the fabricated specimens. To this end, we compare the specimens prepared via the conventional 0.4-mm diameter FFF 3D printer and our HFFF system. In addition, we evaluate the effects of the layer bead width and the in-plane printing raster angle on PLA materials prepared via the HFFF system. A summary of the printing parameter study is given in Table 2. For each group of tests, we prepare eight specimens to eliminate potential artificial errors.
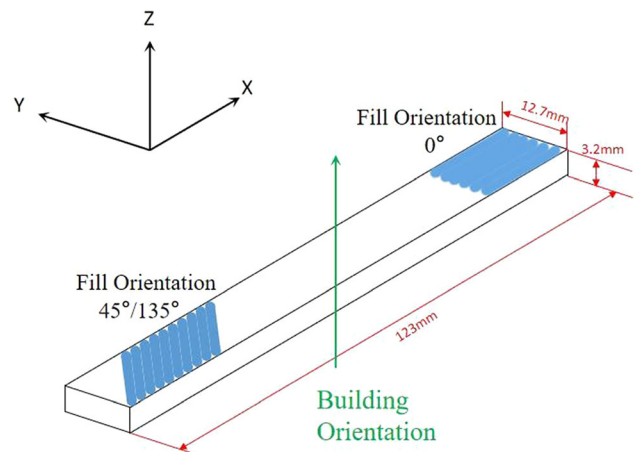

Fig. 5 ASTM-D790 flexural specimen geometry design

Furthermore, we employ thermal characterization for printed specimens via differential scanning calorimetry (DSC-500C, Jiezhun Instrument Equipment Co., Ltd., Shanghai, China) to evaluate the crystallization behaviors. The thermal characterizations are carried out in a nitrogen atmosphere to eliminate potential oxidation contamination. The rate of temperature

Table 2 Printing parameter study of the HFFF system

Filament diameter, mm	Layer bead width, mm	In-plane raster angle, °	Three-dimensional printer	Nozzle temperature, °C	Layer thickness, mm	Print bed temperature, °C
1.75	0.4	45/135	Conventional FFF	220	0.2	50
2.85	1.0	0	HFFF	230	0.4	60
		45/135		230	0.4	60
2.85	0.8	45/135	HFFF	230	0.4	60
	1.0			230	0.4	60
	1.5			230	0.4	60
	2.0			230	0.4	60

increment is set as 10 °C/min. Based on the DSC curves, the crystallinity of the specimen is calculated using Eq. 1 (Ref 40). In the equation, ΔH_m is the enthalpy of the melt peak, ΔH_{cc} is the enthalpy of the cold crystallization peak, ΔH_m^* is the enthalpy of the polymer at 100% crystallization, 93 J g^{-1} (Ref 19), and φ is the weight fraction of the polymer in the tested sample.

$$x_c = \frac{\Delta H_m - \Delta H_{cc}}{\varphi \times \Delta H_m^*} \qquad \text{(Eq 1)}$$

Additionally, we apply the Keyence VHX-7000 digital optical microscope (Keyence Corporation, Osaka, Japan) to explore the microstructural formations of the PLA materials prepared via the HFFF process.

3. Results and Discussion

We employ the PLA material as the feedstock in the entire study. The standard 1.75-mm filaments and enlarged 2.85-mm filaments are provided by Kexcelled Material (Kexcelled New Material Technology Co., Ltd., Suzhou, China) and ZhuoPu Material (Zhuopu New Material Technology Co., Ltd., Hangzhou City, China), respectively. We perform DSC tests on the feedstock materials to ensure that they exhibit highly similar thermal material behaviors, as shown in Fig. 6. The crystallinity of PLA with a wire diameter of 1.75 mm is 4.2%, and the crystallinity of PLA with a wire diameter of 2.85 mm is 1.72%, as calculated by Eq. 1.

In the following section, we present the mechanical testing results of HFFF-produced PLA specimens. In addition, we analyze the mesostructures of the deposited beads, which help explain the variations in the flexural properties of PLA specimens prepared under different processing conditions.

3.1 Flexural Measurement Results

The three-point bending experiment utilizes a sample span of 51.2 mm, as illustrated in Fig. 7, which depicts the setup configuration. The experiment is conducted using a constant speed control mode and a bending rate of 2 mm/min. In the event of failure, the machine is returned to its initial position. Figure 8 presents the average bending strength and stiffness obtained, with the nozzle aperture of a conventional FFF 3D printer set to 0.4 mm. The results indicate a significant improvement in the bending strength of large-volume FFF 3D printing relative to traditional FFF 3D printing. Specifically, in the same 45°/135° printing filling direction, the bending
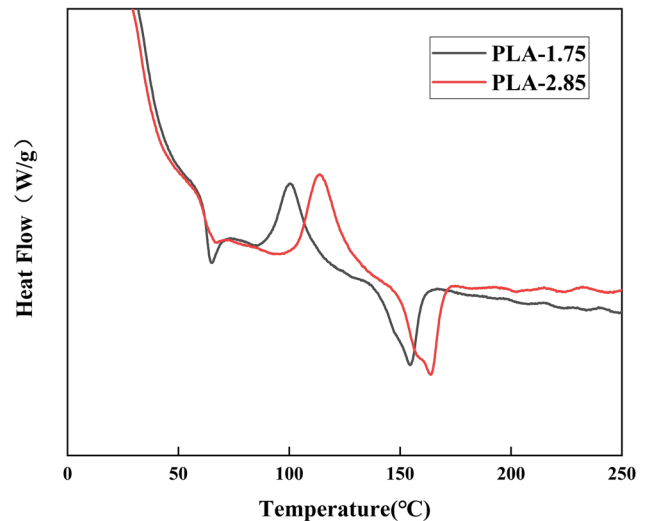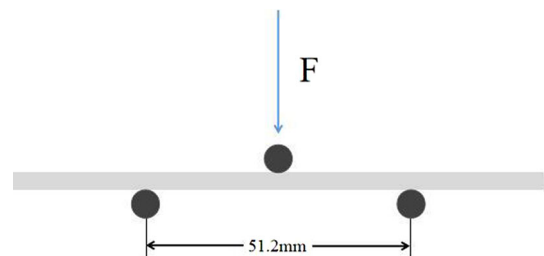

Fig. 6 DSC curves of PLA feedstock materials

Fig. 7 Three-point bending process

strength increases by 8.4 MPa, corresponding to a percentage improvement of 10.04%. Furthermore, under different printing filling directions of 0° and 45°/135°, the bending strength increases by 8.3 MPa, an improvement of 9.92%. It is noteworthy that the bending stiffness remains stable across all relevant parameters. Moreover, Fig. 9 shows a comparison of the bending strength and modulus values of 3D-printed objects with the same printing filling direction and different layer bead widths using the 1-mm nozzle HFFF printer. The comparison indicates that increasing the layer bead width does not necessarily increase the flexural strength. Among the tested layer bead widths, the 1.0-mm width exhibits the highest maximum flexural strength of 92.1 MPa, followed by the 0.8-mm width of 86.1 MPa and the 1.5-mm width of 77.4 MPa.
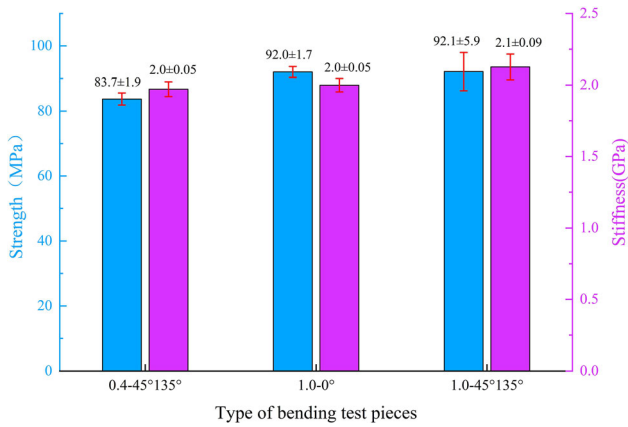
Fig. 8 Comparison of bending strength and stiffness values resulting from FFF and HFFF processes
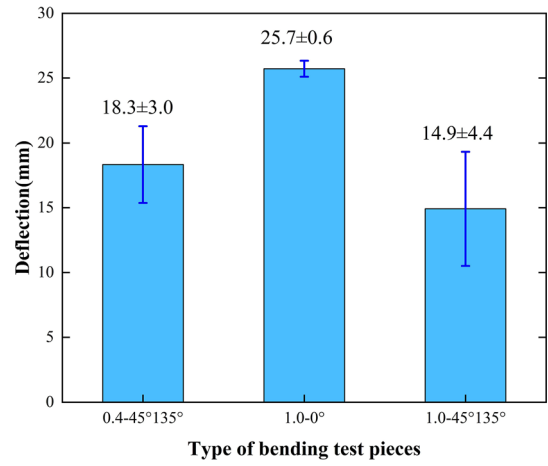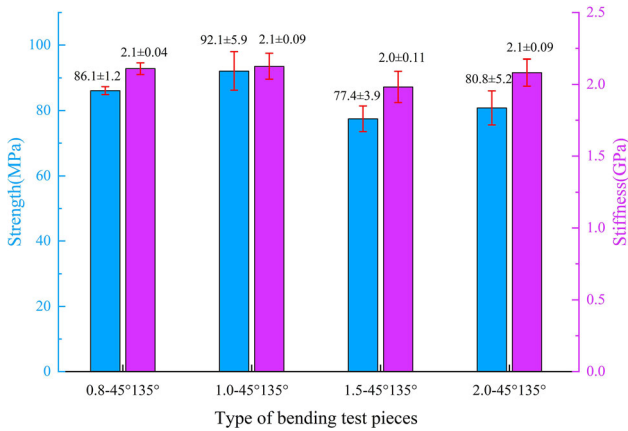

Fig. 9 Comparison of the bending strength and stiffness values of the HFFF-produced specimens with different line widths

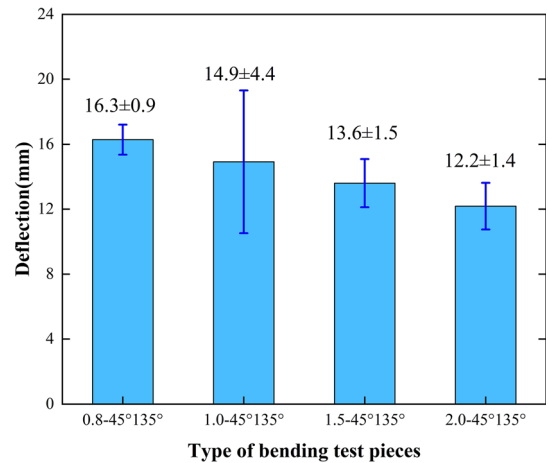However, the stability levels of the mechanical properties decrease with increasing printed bead width. This finding suggests that the properties of 3D-printed objects become decreasingly predictable as the printed bead width increases. Conversely, the bending modulus appears to be unaffected by the considered parameters and remains stable.

Additionally, we analyze the bending deflections of the printed specimens, as shown in Fig. 10 and 11. In Fig. 10, we observe a decrease of 3.4 mm in deflection for the same filling direction of 45°135° and different layer bead widths. The bent part with a 0.4-mm extrusion width exhibits better toughness, whereas the part with a 1.0-mm layer bead width becomes less tough and more brittle. Furthermore, when the filling direction is 0°, the bending deflection increases by 7.4 mm. This increase can be attributed to the printing direction of the bent parts being perpendicular to the load. From Fig. 10 and 11, it is evident that the deflection deformation levels of the specimens with line widths of 0.4 mm, 0.8 mm, 1.0 mm, 1.5 mm, and 2.0 mm decrease by 18.3 mm, 16.3 mm, 14.9 mm, 13.6 mm, and 12.2 mm, respectively. This finding indicates that as the bead width increases, bending stress increases while the deflection of the bending part decreases, resulting in a decrease in toughness.

Finally, Fig. 12 provides a comparison of the print times at a consistent print speed of 40 mm/s. The results demonstrate a significant advantage of HFFF over FFF: faster print times.
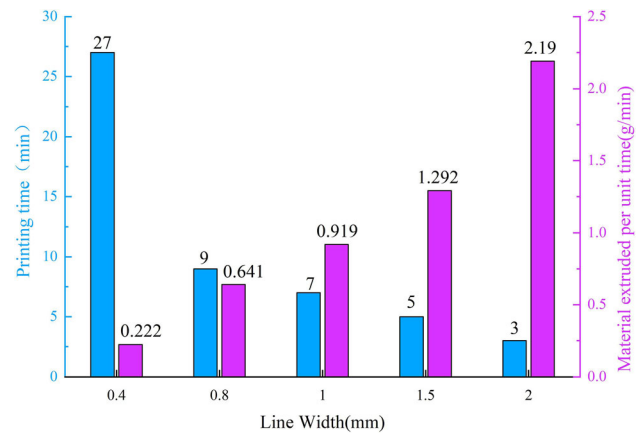

Fig. 10 Comparison of the bending deflections of FFF- and HFFF-produced specimens with different line widths

Fig. 11 Comparison of the bending deflections of HFFF-produced specimens with different line widths

Fig. 12 Printing times for different line widths

This advantage can be attributed to the design of the HFFF system, which utilizes a relatively large nozzle diameter and thick bead width. These design choices enable a higher extrusion flow rate, thereby reducing print time costs. It is

important to note that print time plays a crucial role in many 3D printing applications, particularly in industries where production speed is paramount. The ability to manufacture parts quickly and efficiently can confer a competitive edge, allowing companies to expedite product development and respond quickly to customer demands. Nevertheless, it is vital to recognize that print time is not the sole determinant of the quality and suitability of a 3D-printed part. Other factors, such as strength, durability, and surface finish, hold significance. These factors can be influenced by variables such as material selection, print settings, and postprocessing techniques. In summary, the findings presented in Fig. 12 indicate that HFFF shows promise as an option for applications that emphasize speed and efficiency. However, further research is needed to comprehensively assess the potential advantages and limitations of this printing method. Additionally, it is necessary to compare HFFF with other 3D printing techniques in terms of print quality, cost-effectiveness, and other pertinent factors.

3.2 Mesostructural Analyses

Although HFFF exhibits a promising feature in terms of manufacturing efficiency, the decreased material properties

shown in Fig. 9 indicate that the increased bead width yields negative effects on the resulting flexural performance. To this end, we further explore the mesostructural formations of the printed specimens made with different bead widths, aiming to explain the property reduction shown in Fig. 9. First, Fig. 13 shows the surface roughness values of the specimens prepared under different conditions. Note that the subtitles associated with the subfigures denote the printing bead width filling direction. From the contour plots, the maximum height difference is $\sim 130\ \mu$m (Fig. 13f), and most contours exhibit stable peaks and valleys (which are the bead and interbead voids, respectively). This result indicates that the extrusion rate and flow rate remain stable during the printing of our HFFF system. In addition, Fig. 14 shows the bead width measurements of the printed specimens under different bead width processing conditions. The images are taken via a Keyence microscope. We select the maximum number of deposited beads that can be captured in the field of vision. The measurement results can be automatically generated once we finish the selection of green lines, which denote the board of each deposited bead. When comparing the actual printed bead width with the theoretical values, it is safe to conclude that the customized HFFF printer runs at a stable ex-
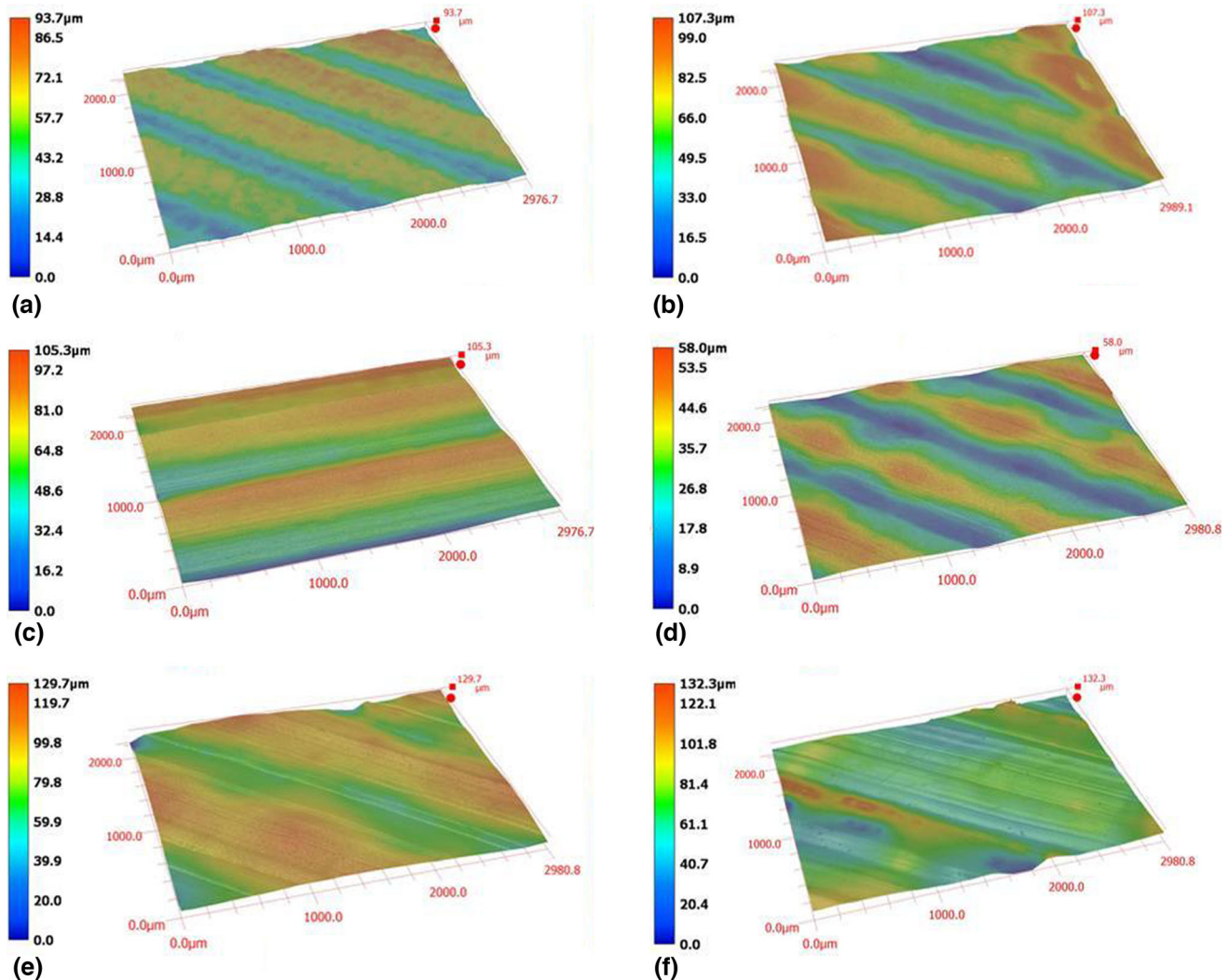

Fig. 13 Surface printing qualities of different bead widths and in-plane raster angles, $100\times$: (a) 0.4 mm-45°135°; (b) 0.8 mm-45°135°; (c) 1.0-0°; (d) 1.0 mm-45°135°; (e) 1.5 mm-45°135°; and (f) 2.0 mm-45°135°
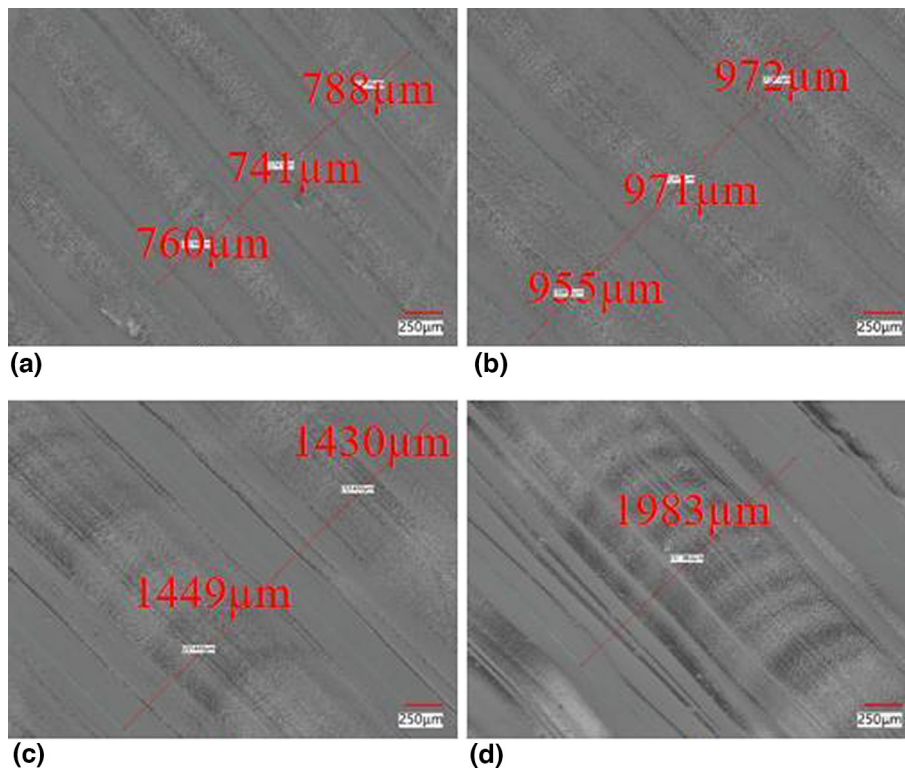
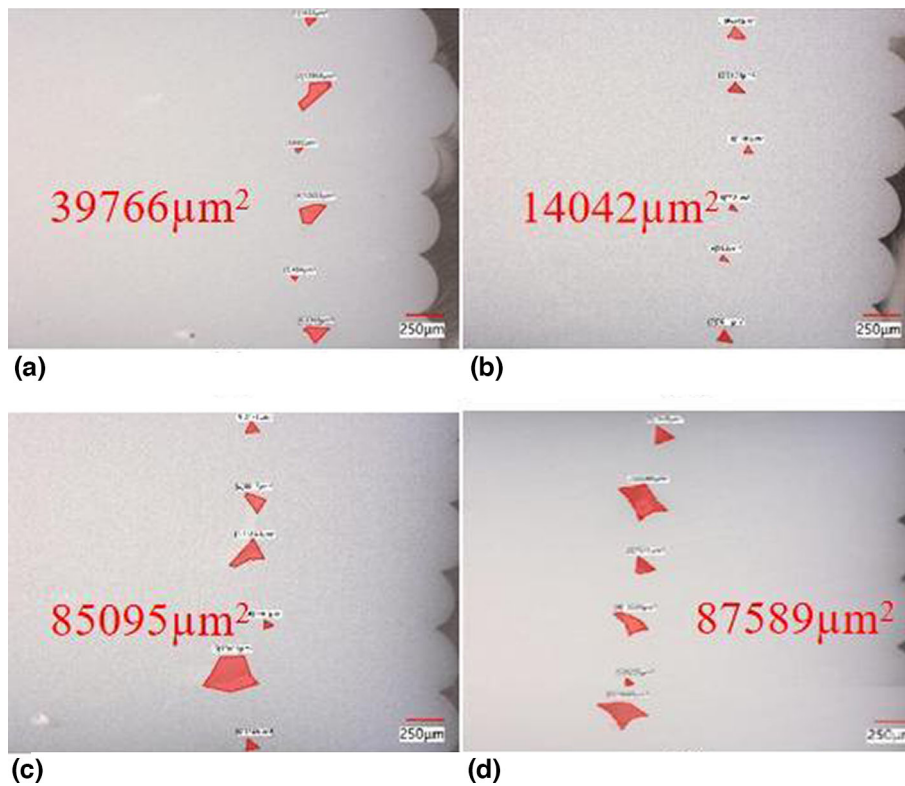**Fig. 14** Different print bead widths, 100× : (a) 0.8 mm; (b) 1.0 mm; (c) 1.5 mm; and (d) 2.0 mm

Fig. 15 Pore areas at different bead widths (and in-plane raster angles are all 45°135°), 100× : (a) 0.8 mm-39,766 μm^2; (b) 1.0 mm-14,042 μm^2; (c) 1.5 mm-85,095 μm^2; and (d) 2.0 mm-87,589 μm^2

trusion rate, as subtle variations are seen between the experimental and theoretical values.

Furthermore, Fig. 15 presents the size of the interlayer pore area, where specimens made with four different bead widths are studied. The bending specimens are cut along the cross-section with slow saws, where roughly one-sixth of the specimen is left. We place the cut sample into a silicone mold and merge it with epoxy resin for 24 h of solidification. After solidification finishes, the surface of the sample is delicately and effectively polished. Finally, a Keyence VH7000 microscope is used to locate pores and measure the dimensions through the operation software directly at $100 \times$ magnification. Here, the first column of interlayer pores is considered since they are much larger than the pores lying among intermediate locations. The red font in the middle of each image is the sum of the area of the six pores, which helps to explain the difference in the bending performance under different bead widths. In addition, Fig. 16 directly compares the pore areas and corresponding bending strengths for all four bead widths. Observing the results, the 1.0-mm bead width demonstrates the least combined pore area at 14,042 μm^2 and a corresponding bending stress of 92.1 MPa. This result is followed by the 0.8-mm bead width, which shows a sum of pore area at 39,766 μm^2 and a corresponding bending stress of 86.1 MPa. Large bead widths, such as 1.5 and 2.0 mm, lead to increased printing fluctuations, resulting in unstable print quality. Deviating from the standard nozzle diameter, whether larger or smaller, amplifies interlayer porosity and leads to premature specimen failure under external bending loads. Moreover, the 1.5- and 2.0-mm bead widths demonstrate a marginal difference in the sum of pore area, amounting to 89,095 and 87,589 μm^2, respectively. With an $\sim 6 \times$ larger pore area, the bending strengths of the 1.5- and 2.0-mm specimens are reduced by 15.9 and 12.3% from that of the 1.00-mm bead width, respectively. To this end, it is considered that the increment of the interlayer porosity directly decreases the flexural performance of HFFF-produced parts, and we expect to further explore the correlation between the printing parameters and the resulting porosity in the future in-depth works.

To gain a scientific view of the effects of different pore sizes on the three-point bending strength, we perform a finite element three-point bending simulation on the specimens. Herein, the
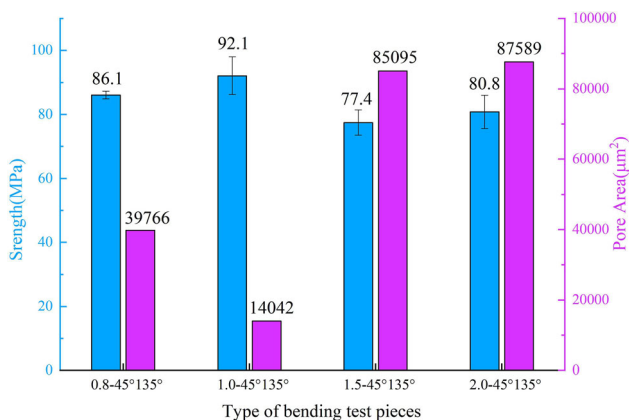
cases of bead widths of 1 and 2 mm are used as an example. The area of each pore in Fig. 15 is mapped to the simulated domain with essential simplifications. For the specimen with a bead width of 1 mm, all the pore shapes are set as triangles, and for that with a bead width of 2 mm, the pore shapes include both triangles and diamonds. The elastic modulus and Poisson's ratio of the modeled PLA are set as 3.1 GPa and 0.36, respectively (Ref 41). We assume perfect bonding between the test tool and the specimen, which results in line contact. At the line of the loading tool, we apply vertical displacements of 1 and 10 mm. Note that the applied strain loads are selected based on our previous experimental results, with the aim of limiting the elastic behaviors of the materials. At the lines of the fixing tools, we apply a three-dimensional fix boundary to the correspondence nodes. All simulations are run with Abaqus/Explicit 2022 (Dassault Systèmes SIMULIA Corp., Providence, RI, USA). The finite element meshes for the 1-mm bead width and 2-mm bead width cases are 174,906 elements with 186,485 nodes and 102,582 elements with 113,867 nodes, respectively.

From the general comparison appearing in Fig. 17, the 1-mm bead width specimen exhibits different stress responses when subjected to 1-mm and 10-mm displacement loads. In addition, by comparing the 1-mm bead width and 2-mm bead width specimen results under the same 1-mm displacement load, it is found that the stress contours vary notably, owing to internal porosity differences. Furthermore, we can observe that when subjected to the same displacement load (1 and 10 mm), the maximum stress of the component with a 1-mm bead width is always greater than that of the component with a 2-mm bead width. Moreover, based on the simulation results shown in the contour plots of Fig. 18, under the condition where the downward displacement is 1 mm for both cases, the following observations can be made: (a) contour plot of the component with a bead width of 1 mm at the middle position of the cross-section; (b) contour plot of the component with a bead width of 1 mm at the bottom left corner (left) support position; and (c) and (d) contour plots of the component with a bead width of 2 mm. Along the path in the contour plot, we generate line graphs of the von Mises stress variation in the test sample along this path (Fig. 19). In general, the stress variation is larger in the middle and smaller at the left support. Finally, Fig. 19 provides the cross-section of von Mises stress contours in the center of the specimen (where the external bending load applies). The legend "strain1-1 mm-median" represents the deformation of the component with a bead width of 1 mm in the middle of the cross-section when subjected to a downward displacement of 1 mm. From the observations in the figure, the maximum stresses are 24 MPa and 20 MPa at bead widths of 1 mm and 2 mm, respectively, indicating an approximate 20% absolute difference between the two. When the downward displacement increases to 10 mm (Fig. 19c), the relative absolute difference is reduced to 2.52%. Based on these analytical results, we can conclude that at the middle position of the component, the 1-mm bead width part can withstand higher bending stresses than the 2-mm bead width part during printing. For Fig. 19(b) and (d), the cross-section is located at the bottom left corner (left) support position. By observing the trend in the line graphs, we can conclude that the printing performance of the 1-mm bead width part is relatively strong. In summary, based on the data and graphs in Fig. 19, we can determine that the component with a 1-mm bead width exhibits more
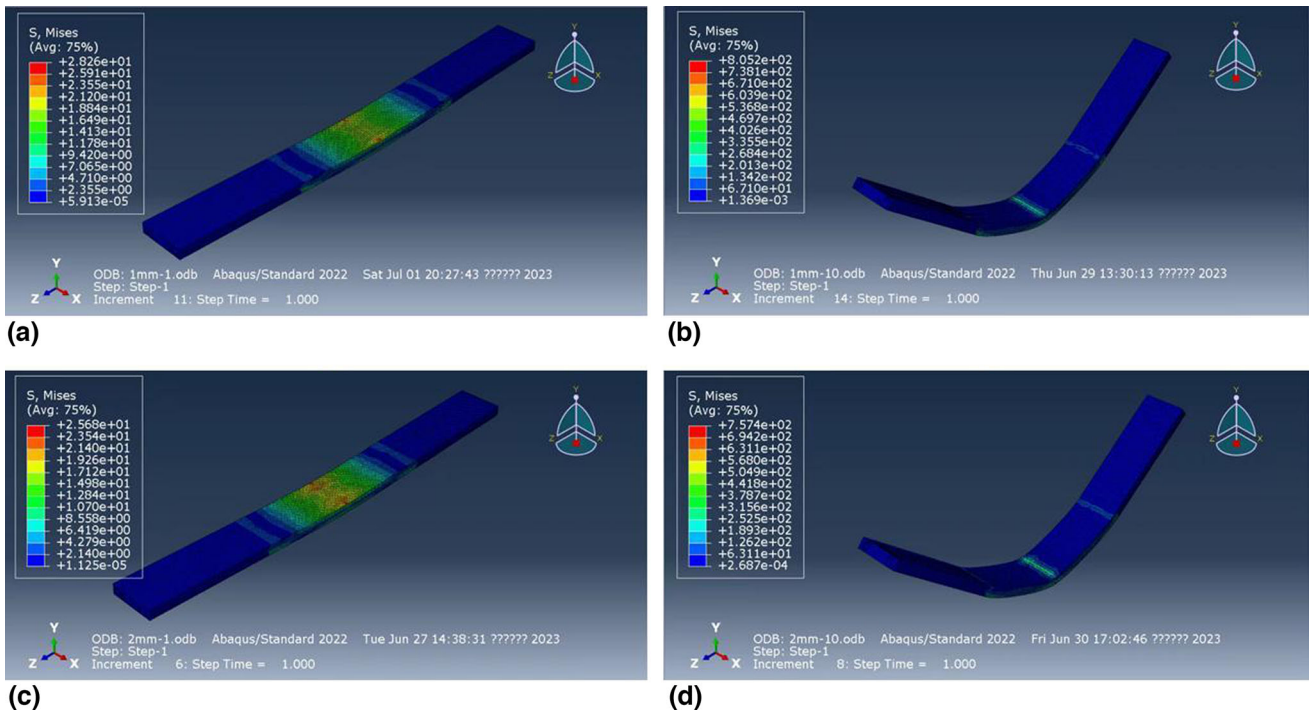

Fig. 16 Pore area versus flexural strength

Fig. 17 von Mises stress (MPa) contours of bending specimens: (a) 1-mm bead width subjected to a 1-mm displacement load; (b) 1-mm bead width subjected to a 10-mm displacement load; (c) 2-mm bead width subjected to a 1-mm displacement load; and (d) 2-mm bead width subjected to 10-mm displacement load
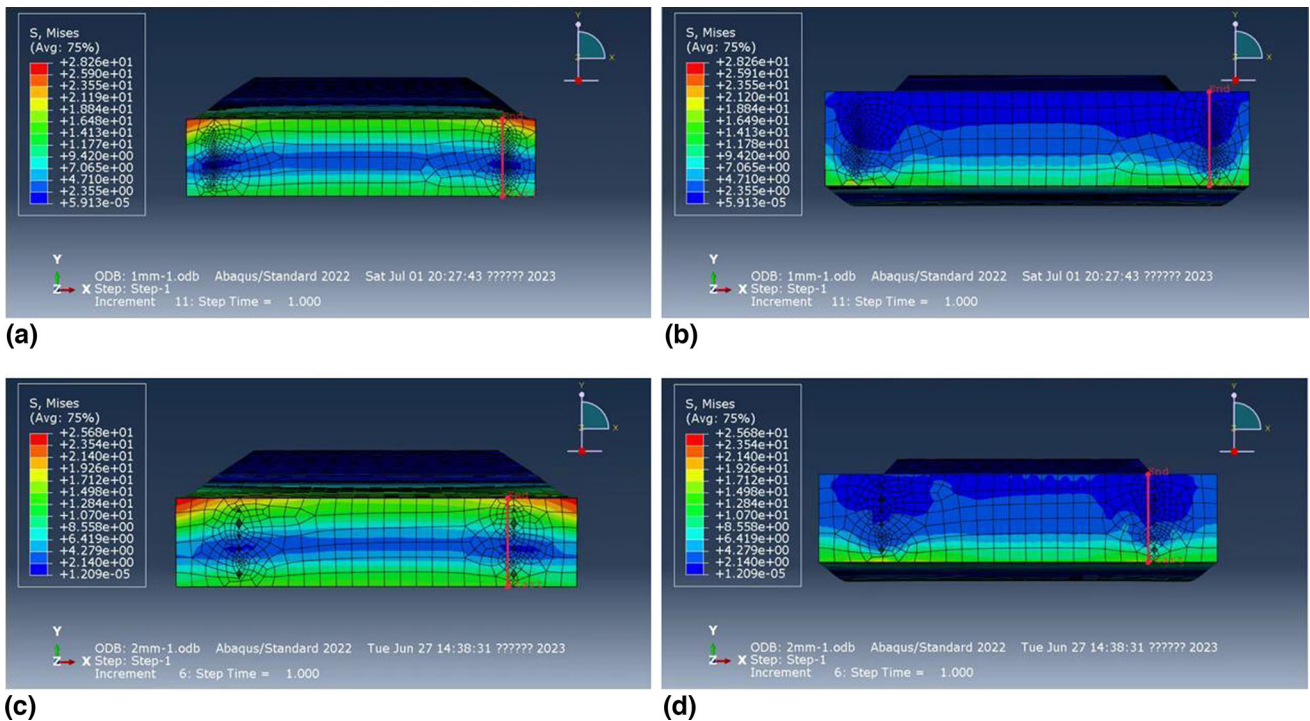

Fig. 18 von Mises stress (MPa) contours of the three-point bending stress simulation: (a) middle of the part with a bead width of 1 mm; (b) bottom left corner of the part with a bead width of 1 mm; (c) middle of the part with a bead width of 2 mm; and (d) bottom left corner of the part with a bead width of 2 mm

favorable performances in terms of the ability to withstand bending loads than the component with a 2-mm bead width.
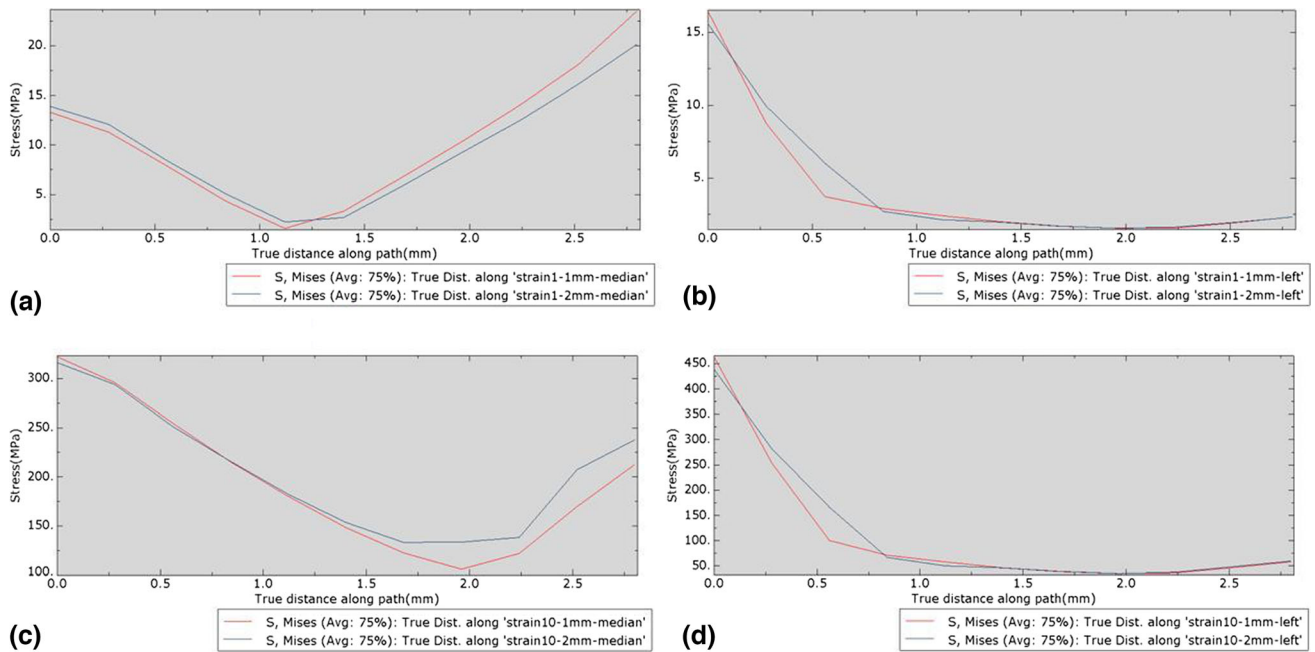
Fig. 19 Stress (MPa) curve of the pore space: (a) 1-mm and 2-mm bead width-1-mm displacement load-middle of the part; (b) 1-mm and 2-mm bead width-1-mm displacement load-bottom left corner of the part; (c) 1-mm and 2-mm bead width-10-mm displacement load-middle of the part; and (d) 1-mm and 2-mm bead width-10-mm displacement load-bottom left corner of the part

4. Conclusions

In this paper, the nozzle diameter of a conventional FFF 3D printer was extended from 0.4 to 1 mm, aiming to increase the volume flow rate for material extrusion. To accommodate the nozzle modification, the extruder was correspondingly modified with a large consumable diameter, high feed pressure, and increased thermal power to support the increased material feeding rate. With the assistance of the presented large-volume FFF 3D printer, we evaluated the flexural properties of PLA materials.

- We first performed preexperiments with PLA filaments with diameters of 1.75 and 2.85 mm. Using the conventional 0.4-mm printer and 1-mm modified HFFF system, we prepared bending specimens with 0.4-mm and 1-mm bead widths, respectively, using the 45°/135° printing filling direction. It was seen that the 1-mm specimens yielded an increment of 10.04% in the bending strength relative to the 0.4-mm specimens, implying the advantages of the HFFF system. Furthermore, the 1-mm specimens with 45°/135° printing filling exhibited slightly higher bending modulus and strength values than those manufactured in the 0° printing filling direction.
- Furthermore, we explored the effects of extrusion bead width on the resulting flexural properties of specimens printed with a 1-mm nozzle. With the help of our HFFF system, specimens were printed separately in four different bead widths (i.e., 0.8, 1.0, 1.5, and 2.0 mm), where the printing filling directions were all set at 45°/135°. The measured data showed that the maximum bending strength of the 1.0-mm extrusion bead width was 92.1 MPa, and the minimum bending strength of the 1.5-mm extrusion bead width was 77.4 MPa, followed by 86.1 MPa for the 0.8-mm width and 80.8 MPa for the 2.0-mm width. The

stiffness did not change significantly, but the bending deflection decreased sequentially as the bead width increased. The maximum deflection of 16.3 mm was observed with the 0.8-mm bead width, while the minimum deflection of 12.2 mm was observed with the 2.0-mm bead width.

- To explain the difference in bending strength among different printing bead widths, we conducted a study on the structural formation characteristics of the failed bending specimens. We used a Keyence microscope to magnify the surface roughness values of the molded parts, the distribution of interlayer pore sizes, and the bead width of the actual printed parts. From the observation of the color depth image, the overall surface quality of the printed parts remained consistent without significant differences in height. The size of the interlayer pore area played a role in explaining the variations in mechanical properties among the four bead widths. The minimum interlayer pore area was 14,042 μm^2, corresponding to a 1.0-mm bead width and a maximum bending strength of 92.1 MPa. This result was followed by a 0.8-mm bead width with an interlayer pore area of 39,766 μm^2, corresponding to a bending strength of 86.1 MPa. The wider pore areas measured 85,095 and 87,589 μm^2, respectively, with little difference in bending strength. The actual printed bead width demonstrated that the HFFF printer was operated with a highly stable extrusion flow, which benefited the performance of the printed parts.

4.1 Remarks

In this study, we explored an alternative approach to large-format additive manufacturing (LFAM), where a conventional FFF 3D printer was modified by using an enlarged nozzle instead of completely changing the material feed system

(typically employing a screw extruder-based feed system as seen in available LFAM systems). The HFFF system we presented aimed to retain most of the features commonly found in standard FFF printers, allowing us to take advantage of the knowledge and insights gained from the FFF community. In this study, we specifically focused on the parameters related to the nozzle. Through our research, we identified an optimal set of processing parameters that led to superior mechanical performance. These findings will inform our future work, where we plan to test our proposed system with fiber-reinforced composites, aiming to achieve efficient and high-performance additive manufacturing technology.

Conflict of interest

The authors declare no conflicts of interest.

References

1. D. Popescu, A. Zapciu, C. Amza et al., FDM Process Parameters Influence over the Mechanical Properties of Polymer Specimens: A Review, *Polym. Test.*, 2018, **69**, p 157–166.
2. J.M. Chacón, M.A. Caminero, E. García-Plaza et al., Additive Manufacturing of PLA Structures Using Fused Deposition Modelling: Effect of Process Parameters on Mechanical Properties and their Optimal Selection, *Mater. Des.*, 2017, **124**, p 143–157.
3. S. Raut, V.K.S. Jatti, N.K. Khedkar et al., Investigation of the Effect of Built Orientation on Mechanical Properties and Total Cost of FDM Parts, *Procedia Mater. Sci.*, 2014, **6**, p 1625–1630.
4. F. Rayegani and G.C. Onwubolu, Fused Deposition Modelling (FDM) Process Parameter Prediction and Optimization Using Group Method for Data Handling (GMDH) and Differential Evolution (DE), *Int. J. Adv. Manuf. Technol.*, 2014, **73**, p 509–519.
5. A.K. Sood, R.K. Ohdar, and S.S. Mahapatra, Parametric Appraisal of Mechanical Property of Fused Deposition Modelling Processed Parts, *Mater. Des.*, 2010, **31**(1), p 287–295.
6. O.A. Mohamed, S.H. Masood, and J.L. Bhowmik, Mathematical Modeling and FDM Process Parameters Optimization Using Response Surface Methodology Based on Q-Optimal Design, *Appl. Math. Model.*, 2016, **40**(23–24), p 10052–10073.
7. A.K. Sood, V. Chaturvedi, S. Datta et al., Optimization of Process Parameters in Fused Deposition Modeling Using Weighted Principal Component Analysis, *J. Adv. Manuf. Syst.*, 2011, **10**(02), p 241–259.
8. R. Narang and D. Chhabra, Analysis of Process Parameters of Fused Deposition Modeling (FDM) Technique, *Int. J. Future Revolut. Comput. Sci. Commun. Eng.*, 2017, **3**(10), p 41–48.
9. T. Nancharaiah, D.R. Raju, and V.R. Raju, An Experimental Investigation on Surface Quality and Dimensional Accuracy of FDM Components, *Int. J. Emerg. Technol.*, 2010, **1**(2), p 106–111.
10. B. Gharehpapagh, M. Dolen, and U. Yaman, Investigation of Variable Bead Widths in FFF Process, *Procedia Manuf.*, 2019, **38**, p 52–59.
11. Q. Sun, G.M. Rizvi, C.T. Bellehumeur et al., Effect of Processing Conditions on the Bonding Quality of FDM Polymer Filaments, *Rapid Prototyp. J.*, 2008, **14**(2), p 72–80.
12. C.P. Khunt, M.A. Makhesana, B.K. Mawandiya et al., Investigations on the Influence of Printing Parameters During Processing of Biocompatible Polymer in Fused Deposition Modelling (FDM), *Adv. Mater. Process. Technol.*, 2022, **8**(sup2), p 320–336.
13. C. Chung Wang, T.W. Lin, and S.S. Hu, Optimizing the Rapid Prototyping Process by Integrating the Taguchi Method with the Gray Relational Analysis, *Rapid Prototyp. J.*, 2007, **13**(5), p 304–315.
14. J. Torres, M. Cole, A. Owji et al., An Approach for Mechanical Property Optimization of Fused Deposition Modeling with Polylactic Acid Via Design of Experiments, *Rapid Prototyp. J.*, 2016, **22**(2), p 387–404.
15. M. Lei, Q. Wei, M. Li et al., Numerical Simulation and Experimental Study the Effects of Process Parameters on Filament Morphology and Mechanical Properties of FDM 3D Printed PLA/GNPs Nanocomposite, *Polymers*, 2022, **14**(15), p 3081.
16. M. Lalegani Dezaki and M.K.A. Mohd Ariffin, The Effects of Combined Infill Patterns on Mechanical Properties in fdm Process, *Polymers*, 2020, **12**(12), p 2792.
17. V. Shanmugam, M.V. Pavan, K. Babu et al., Fused Deposition Modeling Based Polymeric Materials and their Performance: A Review, *Polym. Compos.*, 2021, **42**(11), p 5656–5677.
18. B.N. Panda, K. Shankhwar, A. Garg et al., Performance Evaluation of Warping Characteristic of Fused Deposition Modelling Process, *Int. J. Adv. Manuf. Technol.*, 2017, **88**, p 1799–1811.
19. N.A. Sukindar, M.K.A. Ariffin, B.H.T. Baharudin et al., Analyzing the Effect of Nozzle Diameter in Fused Deposition Modeling for Extruding Polylactic Acid Using Open Source 3D Printing, *J. Teknol*, 2016, **78**(10), p 7–15.
20. W. Kiński and P. Pietkiewicz, Influence of the Printing Nozzle Diameter on Tensile Strength Of Produced 3D Models in FDM Technology, *Agric. Eng.*, 2020, **24**(3), p 31–38.
21. I. Buj-Corral, A. Bagheri, A. Domínguez-Fernández et al., Influence of Infill and Nozzle Diameter on Porosity of FDM Printed Parts with Rectilinear Grid Pattern, *Procedia Manuf.*, 2019, **41**, p 288–295.
22. L. Yang, S. Li, Y. Li et al., Experimental Investigations for Optimizing the Extrusion Parameters on FDM PLA Printed Parts, *J. Mater. Eng. Perform.*, 2019, **28**, p 169–182.
23. F. Chen, Q. Xu, F. Huang et al., Effect of Nozzle Vibration at Different Frequencies on Surface Structures and Tensile Properties of PLA Parts Printed by FDM, *Mater. Lett.*, 2022, **325**, 132612
24. P. Czyżewski, D. Marciniak, B. Nowinka et al., Influence of Extruder's Nozzle Diameter on the Improvement of Functional Properties of 3D-Printed PLA Products, *Polymers*, 2022, **14**(2), p 356.
25. H.L. Brooks. Variable fused deposition modelling-concept design and tool path generation (2011)
26. G. Hodgson, A. Ranellucci, and J. Moe. Slic3r manual—flow math. Aleph Objects 1 (2016)
27. P. Xu, M. Hu, N. Li et al., Magnetic Controlled Variable Diameter Nozzle for Wood Powder 3D Printer, *Revista tecnica de la facultad de ingenieria Universidad del zulia*, 2016, **39**(8), p 77–84.
28. M.D. Monzón, I. Gibson, A.N. Benítez et al., Process and Material Behavior Modeling for a New Design of Micro-additive Fused Deposition, *Int. J. Adv. Manuf. Technol.*, 2013, **67**, p 2717–2726.
29. T.Y. Wang, L.W. Chang, F. Yen-Bor, et al. Feeding device and variable squeezing mouth for 3d printing: U.S. Patent Application 15/389,141[P]. 2018-6-7
30. H.S. Ramanath, C.K. Chua, K.F. Leong et al., Melt Flow Behaviour of Poly-ε-caprolactone in Fused Deposition Modelling, *J. Mater. Sci. Mater. Med.*, 2008, **19**, p 2541–2550.
31. V.E. Kuznetsov, A.G. Tavitov, O.D. Urzhumtsev et al., Desktop Fabrication of Strong Poly (Lactic Acid) Parts: FFF Process Parameters Tuning, *Materials*, 2019, **12**(13), p 2071.
32. B. Nowak and J. Pająk. Biodegradacja polilaktydu (PLA) (2010)
33. F. Pignatelli and G. Percoco, An Application-and Market-Oriented Review on Large Format Additive Manufacturing, Focusing on Polymer Pellet-Based 3D Printing, *Prog. Addit. Manuf.*, 2022, **7**(6), p 1363–1377.

34. D. Moreno Nieto and S.I. Molina, Large-Format Fused Deposition Additive Manufacturing: A Review, *Rapid Prototyp. J.*, 2020, **26**(5), p 793–799.

35. C. Ajinjeru, V. Kishore, P. Liu et al., Determination of Melt Processing Conditions for High Performance Amorphous Thermoplastics for Large Format Additive Manufacturing, *Addit. Manuf.*, 2018, **21**, p 125–132.

36. J. Butt, R. Bhaskar, and V. Mohaghegh, Investigating the Effects of Extrusion Temperatures and Material Extrusion Rates on FFF-Printed Thermoplastics, *Int. J. Adv. Manuf. Technol.*, 2021, **117**(9–10), p 2679–2699.

37. P. Geng, J. Zhao, W. Wu et al., Effects of Extrusion Speed and Printing Speed on the 3D Printing Stability of Extruded PEEK Filament, *J. Manuf. Process.*, 2019, **37**, p 266–273.

38. Z. Jin, Z. Zhang, and G.X. Gu, Autonomous In-Situ Correction of Fused Deposition Modeling Printers Using Computer Vision and Deep Learning, *Manuf. Lett.*, 2019, **22**, p 11–15.

39. ASTM D790-17 Standard Test Methods for Flexural Properties of Unreinforced and Reinforced Plastics and Electrical Insulating Materials, ASTM International, West Conshohocken, PA (2014)

40. L.S. De Bortoli, R. De Farias, D.Z. Mezalira et al., Functionalized Carbon Nanotubes for 3D-Printed PLA-Nanocomposites: Effects on Thermal and Mechanical Properties, *Mater. Today Commun.*, 2022, **31**, 103402

41. P. Żur, A. Kołodziej, and A. Baier, Finite Elements Analysis of pla 3d-Printed Elements and Shape Optimization, *Eur. J. Eng. Sci. Technol.*, 2019, **2**(1), p 59–64.